RSC Advances

PAPER

View Article Online
View Journal | View Issue

Cite this: *RSC Adv.*, 2026, **16**, 22627

Tunable gas sensing features of Janus In_2STe monolayers: insights from first-principles and multiphysics studies on SO_2 interaction

Raiyan Al Nahean, †[a] Md. Raiyan Firoz,†[a] Manik Bala[ab] and Md Tawabur Rahman *[a]

The detection of hazardous gases plays a critical role in both industrial and healthcare applications. MOS (metal oxide semiconductor) sensors have been extensively studied in gas sensing applications, but they have low selectivity, require higher working temperatures, and use a lot of power. This work investigates the sensing and adsorption properties of hazardous gases (NH_3, SO_2, H_2S, NO_2, HCN, and CO_2) on a Janus In2STe monolayer using first-principles density functional theory (DFT) calculations and COMSOL Multiphysics modeling. First-principles analyses reveal that SO_2 is chemisorbed on In_2STe, while the other gases are physisorbed. Among all the adsorbed gases, SO_2 exhibits the highest adsorption energy (−0.82 eV), which suggests the strongest interaction with the Janus In_2STe monolayer. The sensor based on this monolayer shows a remarkable chemiresistive sensitivity (93.28×10^6%) and a suitable recovery time (74 seconds) for SO_2, significantly outperforming other gases. Additionally, a sensor incorporating the Janus In_2STe monolayer as the sensing layer was simulated using COMSOL to validate these findings further. At room temperature (RT), Janus In_2STe showed a high response (R_a/R_g) of 17.62 to 50 ppm of SO_2, an impressive sensitivity of 0.308 ppm^{-1}, and excellent selectivity for SO_2 in mixed gas environments, surpassing conventional gas sensors. These results offer valuable insights for the manufacture of low-power-consuming and selective gas sensors and emphasize their potential for predictive modeling in guiding sensor design before synthesis.

Received 24th December 2025
Accepted 14th April 2026

DOI: 10.1039/d5ra09962e

rsc.li/rsc-advances

1. Introduction

One of the most significant environmental issues of our day is the ongoing increase in harmful air pollutants, which are mostly released from sources like transportation, industrial facilities, refineries, asbestos-containing building materials, tobacco smoke, and chemical solvents.[1] These hazardous gases and vapors can pose serious health risks to individuals, especially workers, through inhalation, skin contact, or ingestion.[1] Consequently, appropriate and timely sensing of such gases is important not only for environmental monitoring but also for ensuring personal safety and enhancing industrial process control.

While traditional MOS-based gas sensors have shown excellent selectivity, they often fall short in detecting gases at low concentrations due to limited sensitivity.[2] 2D materials show great promise for applications in chemical detection due to their great surface-to-volume proportion, along with their ability to operate effectively at room temperature.[3] Among them, Group III chalcogenide monolayers (MX, where M = Ga or In and X = Te, Se, or S) have garnered significant attention for use in next-generation nanoelectronic and optoelectronic devices.[4] This interest stems from their unique multilayered configuration, in which a double layer of Group III metal atoms is sandwiched between two chalcogen atom layers.[4] A further advancement in this domain is the development of Janus 2D materials, which possess out-of-plane structural asymmetry. These materials are synthesized by substituting either the top and bottom chalcogen layers or the central Group III metal layers with different elements. Phonon spectrum analyses confirm the dynamic stability of these Janus monolayers.[5] In gas detection, Janus materials have demonstrated remarkable promise for achieving both high sensitivity and selectivity. For instance, various gases can be adsorbed onto MoSSe Janus structures, with NO_2 and SO_2 showing especially strong affinities for Se- and S-sites.[6] Similarly, the Janus B_2SeTe monolayer demonstrates chemsorption behavior for NO_2, while NH_3, SO_2, H_2S, CH_4, CO, CO_2, and HCN were chemisorbed on this material.[7]

Motivated by these findings, our work aims to explore Janus In_2STe's gas detection potential, as there is no prior research on the gas detection mechanism of Janus In_2STe. This work

[a]*Department of Electrical and Electronic Engineering, Khulna University of Engineering & Technology, Khulna-9203, Bangladesh. E-mail: tawabur@eee.kuet.ac.bd*

[b]*Department of Electrical and Electronic Engineering, Bangladesh Army University of Engineering & Technology (BAUET), Natore, Bangladesh*

† Equally contributed authors.

involves a DFT analysis of the adsorption configuration and sensing mechanism of six gases on the In_2STe monolayer. DFT-based analyses revealed that SO_2 undergoes chemisorption, whereas other gases are physisorbed on the surface. The In_2STe monolayer demonstrated an exceptional chemiresistive sensitivity of 93.28×10^6% and a suitable recovery time (74 seconds) at RT for SO_2, significantly outperforming its response to the other two gases. Additionally, COMSOL Multiphysics was employed to simulate and model a gas sensor incorporating In_2STe as the sensing layer. At RT, the Janus In_2STe showed a markedly higher response ($R_a/R_g = 17.62$) to SO_2 compared to NH_3 and H_2S. These results help the development of optimal sensor designs for high-performance gas detection and offer significant insights into the gas detection mechanism.

2. Methodology

2.1 Computational analysis in DFT

The electronic and structural optimization has been calculated employing *ab initio* simulations. The CASTEP (Cambridge Serial Total Energy Package) program was employed to perform computations.[8] The GGA and the PBE functional have been utilized in elucidating the interplay between exchange and correlation potentials. For geometry optimization, the 'Grimme' method has been utilized for DFT-D3 correction.[7,9] A $3 \times 3 \times 1$ supercell of In_2STe monolayer was constructed for the simulations, including gas molecules adsorbed on the surface.

450 eV is set as the energy cutoff. Largest displacement and highest stress are set to 0.001 Å and 0.05 GPa, respectively. And, the highest force and convergence tolerance energy are fixed at 1.0×10^{-6} eV per atom and 0.01 eV $Å^{-1}$, respectively. Cell optimization was performed using a fixed basis quality to ensure reliable performance under hard compressibility and varying cell parameters. While we employed the relativistic Koelling–Harmon method for computing electrical characteristics, we opted for the Norm Conserving methodology for pseudopotentials. The BFGS algorithm was used to optimize geometry. Additionally, we selected a $6 \times 6 \times 1$ k-point set for geometry optimization and the computation of electronic properties.[4]

Eqn (1) has been used in calculating the adsorption energy under the gas adsorption.[10]

$$E_{ad} = E_{(In_2STe+gas)} - E_{In_2STe} - E_{gas} \quad (1)$$

E_{ad} represents the adsorption energy arising from the attachment of gas molecules to the sensing surface. The energy of Janus In_2STe under gas absorption is indicated by $E_{(In_2STe+gas)}$. The energy of Janus In_2STe and gas is denoted by E_{In_2STe} and E_{gas}, respectively. To determine the charge density difference (CDD) during gas adsorption, eqn (2) was used. Here, ρ_m, ρ_{gas}, and ρ_{total} denote the charge density of Janus In_2STe, the gas molecule, and gas-adsorbed In_2STe, respectively.

$$\Delta\rho = \rho_{total} - \rho_m - \rho_{gas} \quad (2)$$

The shift in electrical conductivity (σ) is an important consideration in determining gas sensing's effectiveness. The equation below explains how conductivity and band gap, E_g, are related,[2,4]

$$\sigma = A \exp\left(-\frac{E_g}{2k_B T}\right) \quad (3)$$

In this case, the proportionality constant, band gap, Boltzmann constant in eV K^{-1}, and temperature in Kelvin are denoted by A, E_g, k_B, and T.

The charge transfer difficulty of the system increases in proportion to the electronic bandgap, according to molecular orbital theory. A rise in the band gap makes it harder for electrons to shift from the valence to the conduction band, as conductivity and band gap share an inverse relationship (resistance increases).[11]

The chemiresistive sensitivity of the sensing material is defined by the following equation,[12]

$$\%S\left(\frac{\delta\sigma}{\sigma}\right) = \left|\frac{\exp\left(-\frac{E_g\ (\text{adsorbed})}{2k_B T}\right) - \exp\left(-\frac{E_g\ (\text{pristine})}{2k_B T}\right)}{\exp\left(-\frac{E_g\ (\text{pristine})}{2k_B T}\right)}\right| \times 100 \quad (4)$$

Here, E_g (adsorbed) and E_g (pristine) denote the bandgap of Janus In_2STe under gas adsorption and that of pristine In_2STe. The recovery period is defined as the duration required for gas molecules to naturally detach from the sensing surface. The recovery time has been calculated using the Van't Hoff–Arrhenius equation, which is given below.[2,13,14]

$$\tau = \nu_0^{-1} \exp\left(-\frac{E_{ad}}{k_B T}\right) \quad (5)$$

Here, ν_0 is the attempt frequency. Previous studies suggest that the attempt frequency for SO_2 is on the order of 10^{12} s^{-1}. However, for all other gases, the same value of frequency can be used.[2,15]

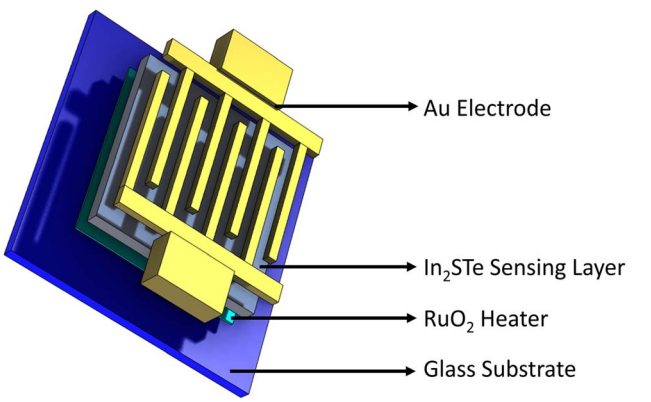

Fig. 1 The IDE structure of the proposed gas sensor.

2.2 Sensor modeling and simulation in COMSOL

Fig. 1 depicts the Janus In_2STe material-based sensor structure modeled in COMSOL Multiphysics. The structure of the proposed sensor consists of 4 main parts, namely:

(a) Glass substrate: it is considered to have dimensions of 15 × 15 × 0.7 mm^3.

(b) Sensing layer: the heart of the sensor, which is made up of Janus In_2STe material having an area of 10 × 10 mm^2. The thickness of the proposed sensing layer is considered to be 0.85 mm, which is sufficient for good response characteristics.

(c) Interdigitated electrodes (IDEs): the gold (Au) IDEs structure is used to obtain a reproducible response from the sensor. Additionally, two Au contacts are used to collect charges from the sensing layer as a result of the gas–material interaction.

(d) Heater: to fasten the reaction process, a ruthenium oxide-based heater is being considered, which has the same dimensions of 10 × 10 mm^2 as the sensing layer.

Additionally, for simulating gas flow, a cylindrical chamber with a gas sensor enclosed is considered, with a 15 mm diameter and a height of 20 mm. This chamber also has two outlets with a radius of 2 mm. The gas sensing measurement was conducted in this enclosed chamber, where the gas enters through the inlet and is subsequently collected at the outlets.[16]

During the simulation, SO_2 gas at different concentrations was introduced through the inlet into the chamber and exposed to the sensor surface for approximately 20 seconds, allowing the simulation of the corresponding dynamic response. Before each measurement, any residual gas in the chamber was removed. To simulate the whole process accurately, COMSOL Multiphysics has been utilized to solve partial differential equations and their corresponding physics interfaces.[7]

The gas flow inside the chamber is described using the Navier–Stokes equation,[17]

$$\rho = -\nabla P + \rho g + \eta \nabla^2 \tag{6}$$

Here, ρ, P, η, g, and U denote gas flux, gas pressure, viscosity, gravity, and velocity field, respectively. The solution of these equations has to be done using the continuity equation in order to ascertain the gas velocity and field.[18]

$$\rho + \nabla(\rho U) = 0 \tag{7}$$

The equation can be written as follows, assuming incompressible gas flow, where the density remains constant.[19]

$$\nabla U = 0 \tag{8}$$

$$U_T = 0 \tag{9}$$

The cylindrical chamber's surfaces are in a state of zero relative velocity, where the peripheral velocity is indicated by U_T.

Fourier's law states that a material's negative temperature gradient directly affects how quickly heat is transferred through it.[20]

$$q'' = -k \times T \times \nabla \tag{10}$$

Here, T indicates the temperature, and q'' denotes flux density. And, thermal conductivity is denoted by k. The following equation represents conductivity σ as follows,[21]

$$\sigma = en\mu \tag{11}$$

Here, μ, n, and e are the mobility, carrier concentration, and charge, respectively. Although both eqn (3) and (11) represent electrical conductivity, they originate from different physical considerations. Eqn (11) describes conductivity in terms of charge transport, where σ depends directly on the carrier concentration (n) and mobility (μ), meaning it reflects how effectively existing charge carriers move through the material.[22,23] In contrast, eqn (3) expresses conductivity in terms of the band gap and temperature, emphasizing the thermal generation of charge carriers in a semiconductor. In this case, the exponential dependence arises from the probability of electrons being excited across the band gap.[4,24] The conducting layer of the sensor alters when it comes into contact with a gas having a concentration C, indicated by the following,[17]

$$\sigma = (n - \alpha C t)e\mu \tag{12}$$

Here, α and t denote the adsorption coefficient and the active layer's per-unit surface area. The modified form of the above formula has been written as follows,[16]

$$\sigma = e\mu(n - \alpha \Delta t) \tag{13}$$

With the increase of gas concentration, Δt increases and eventually reaches saturation. Δt decreases as the concentration lowers. Resistivity ρ can be expressed as,[20]

$$\rho = \frac{1}{\sigma} = \frac{1}{(n - \alpha C t)^2 e\mu} \tag{14}$$

Thus, conductivity and resistivity will change when SO_2 is adsorbed onto the sensing layer.

The TDS (Transport of Diluted Species) module was used to model the movement and interaction of SO_2 molecules towards the sensing layer. It accounts for the convection mechanism within the defined domain.[18]

The In_2STe sensor's response is measured as (R_a/R_g). Here, R_a indicates the sensor's resistance in air. And R_g is the sensor's resistance in exposure to the gas.

The duration for a sensor exposed to the gas to achieve 90% of its maximal response is known as response time (T_{res}). Conversely, the recovery period (T_{rec}) is the duration, after the target gas is removed, for the response to fall to its maximum value's 10%.[25]

A complementary study was carried out to design interdigitated electrodes (IDEs) with varying geometric parameters and to quantify how these parameters affect sensor response. A series of IDE geometries was constructed by varying finger width and the number of fingers to evaluate sensitivity. Device performance was assessed by examining the electric-field distribution within and around the electrode gap, which serves as a proxy for sensor sensitivity. The Electrostatics interface of COMSOL Multiphysics' AC/DC module was used for

all simulations. In this formulation, the electric displacement field D, the electric field E, and the scalar voltage V are related by Gauss's law and the constitutive relation:

$$\nabla.D = \rho \quad (15)$$

$$E = -\nabla V \quad (16)$$

$$D = \varepsilon_r \varepsilon_0 E \quad (17)$$

Here, V denotes the electric potential, E and D represent the electric field and the electric displacement field, respectively. The relative permittivity is given by ε_r, and ε_0 denotes the free space permittivity. The term ρ corresponds to the free charge density present in the domain.

We conducted two sets of simulations to systematically explore the geometric parameters' influence. In the first set, the finger width was varied between 0.2 mm and 0.6 mm to determine the configuration exhibiting the highest sensitivity. The most responsive design from this stage was then utilized in the subsequent set of simulations, where the number of fingers was varied from 3 to 6. Following each simulation, the IDE configuration demonstrating optimal performance based on electric field distribution and sensitivity metrics was selected for further analysis and integration into the overall sensor model.

The sensor was meshed by considering a coarse element size with a physics-controlled sequence type.

3. Results and discussion

3.1 Structural optimization of the Janus In_2STe monolayer

Fig. 2(a) and (b) depict the top and side views of Janus In_2STe after geometry optimization. The best adsorption site was then identified by introducing gas molecules to the adsorption sites that were being considered. The thickness (t) of the optimized Janus In_2STe is calculated to be 5.37 Å. The unit cell's lattice constant is $a = b = 4.16$ Å. Fig. 2(b) displays that, in optimized In_2STe, the bond lengths of In–S (d_1), In–In (d_2), and In–Te (d_3) are 2.53 Å, 2.73 Å, and 2.75 Å, respectively. The bond angles of In–S–In (θ_1), In–Te–In (θ_2), S–In–In (θ_3), and Te–In–In (θ_4) are 103.36°, 92.19°, 115.02°, and 123.72°, respectively. These are almost identical to those in the previously reported work.[26]

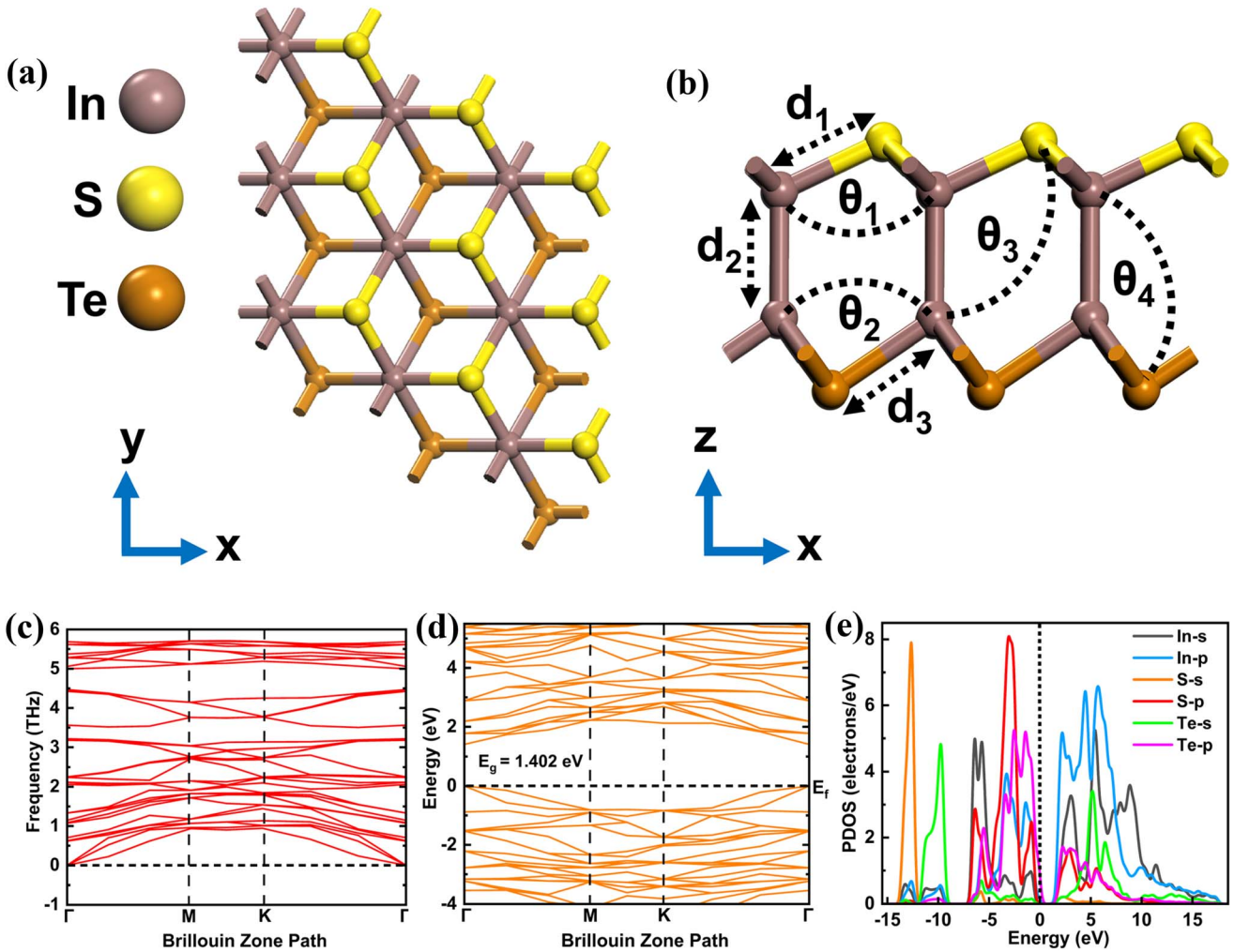

Fig. 2 (a) Top view, (b) side view, (c) the phonon dispersion curve, (d) band structure, and (e) PDOS of the optimized In_2STe monolayer.

Fig. 2(c) exhibits the phonon dispersion of Janus In_2STe through the path of Γ–M–K–Γ. It confirms the dynamical stability of In_2STe due to the absence of imaginary frequencies in the Brillouin zone. The three lowest branches are acoustic modes. These are transverse acoustic, longitudinal acoustic, and a quadratic out-of-plane acoustic mode, which is a typical feature of 2D materials. The higher branches correspond to optical modes, with frequencies extending up to ~6 THz,

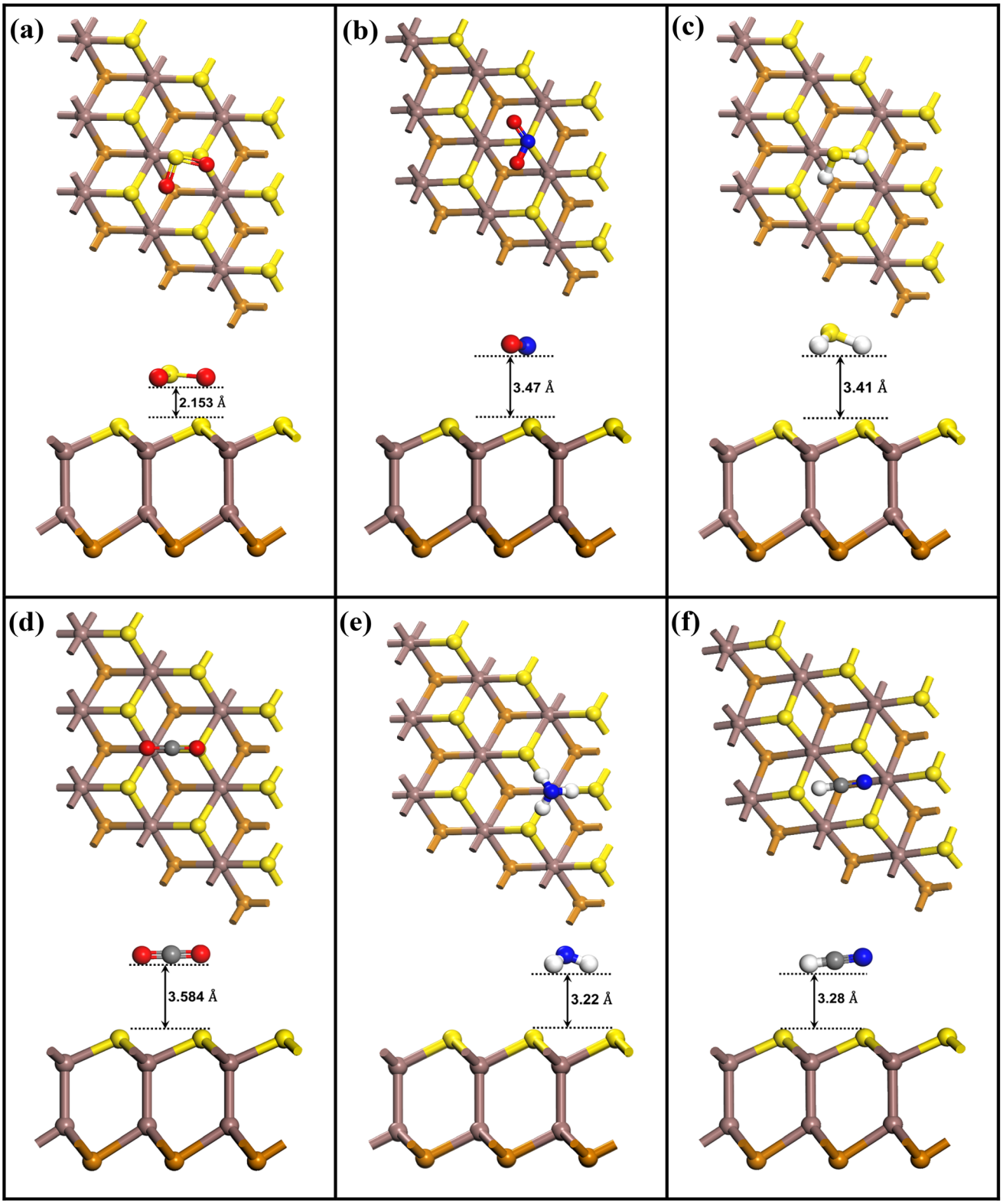

Fig. 3 Adsorption configurations of (a) SO_2, (b) NO_2, (c) H_2S, (d) CO_2, (e) NH_3, and (f) HCN on Janus In_2STe.

indicating moderately strong In–S and In–Te bonding. The absence of imaginary modes ensures the structure is robust, while the built-in polarity from the Janus asymmetry may lead to LO-TO splitting at Γ and influence thermal and electronic transport properties. Overall, the phonon spectrum reflects a stable, polar 2D semiconductor with moderate lattice dynamics. The electronic band structure of Janus In_2STe is shown in Fig. 2(d) along the same path as that of the phonon dispersion. The bandgap (GGA-PBE) of Janus In_2STe is 1.402 eV. Janus In_2STe has a direct band gap, as the conduction band minimum (CBM) and valence band maximum (VBM) are at the same Γ point. Fig. 2(e) displays the optimized Janus In_2STe's PDOS (partial density of states), where the p orbitals of S and Te dominate the valence band region below the Fermi level, with In-s states contributing less. With a small amount of hybridization from Te-s and S-p states, In-p orbitals account for the majority of the CB region above the Fermi level. This shows that In_2STe's optical and electronic characteristics are defined by electronic transitions across the band gap between S-p and Te-p levels in the VB and In-p states in the CB. Since Te-derived states dominate the valence band maximum, Te atoms significantly influence the electronic properties of the material. In a practical device, interaction with an underlying substrate (*e.g.*, glass) may introduce minor interfacial effects such as weak coupling, strain, or slight charge redistribution, which could moderately influence the electronic states near the Fermi level. However, since glass substrates are typically amorphous and electronically inactive, their overall impact is expected to be limited and unlikely to significantly change the intrinsic sensing behavior.[27,28] Therefore, the sensing performance is mainly controlled by the active Te surface sites' interaction with gas molecules. The lattice constant, bond lengths, bond angles, thickness, bandgap, related VBM and CBM locations, and stability for the Janus In_2STe monolayer are all listed in Table SI.

3.2 Adsorption configurations of the Janus In_2STe

Eqn (1) was used to get the corresponding adsorption energies after the gases and their adsorbed structures were initially optimized. The most stable and energetically advantageous gas adsorptions on Janus In_2STe are depicted in Fig. 3 and were chosen for additional analysis. To determine the most stable adsorption configurations, we carefully examined several possible adsorption sites on the Janus In_2STe surface, including the top of In, S, and Te atoms, and bridge sites (In–S and In–Te bonds). For each site, different initial orientations of the gas molecules were considered, and all structures were fully optimized using DFT until the convergence criteria were met. The configuration with the lowest total energy among the tested structures was selected as the most stable adsorption site, representing locally stable minima on the potential energy surface. While it is computationally challenging to guarantee identification of the absolute global minimum across the entire potential energy surface, this systematic multi-site and multi-orientation approach is commonly used and provides a reliable estimation of the most favorable adsorption

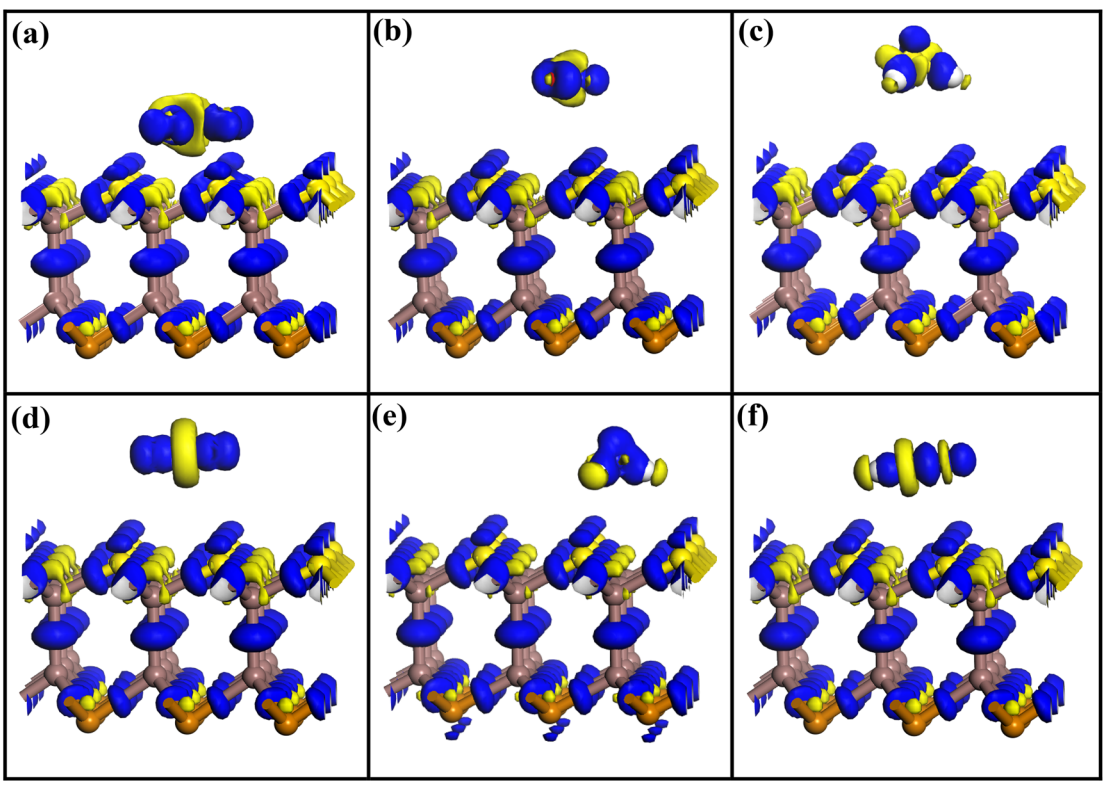

Fig. 4 Charge density difference (CDD) plots for (a) SO_2, (b) NO_2, (c) H_2S, (d) CO_2, (e) NH_3, and (f) HCN adsorbed on the Janus In_2STe monolayer. The blue region signifies electron accumulation, while depletion is indicated by the yellow region.

configuration.[29,30] Each gas molecule has a distinct orientation and favors a particular adsorption site on the Janus In_2STe, as shown in the figure. The shortest lengths between Janus In_2STe and gas molecules also differ as a result of these variances. This distance (D) is a crucial factor that clarifies the kind of interaction between In_2STe and the gas molecules. Both the charge transfer and adsorption energy were computed to comprehend the type of adsorption. Chemisorption is typically indicated if the adsorption energy is less than −0.5 eV, or more negative.[4,31] The shorter adsorption distances (typically from 1.5 to 2.5 Å) correspond to chemisorption, while the larger adsorption distances (usually greater than 2.5 Å) correspond to physisorption.[32–34] The adsorption patterns and associated adsorption behavior of the gas molecules are discussed in the next section.

3.2.1 SO_2. The large adsorption energy (−0.82 eV) resulting from SO_2 adsorption on Janus In_2STe suggests that SO_2 adsorption is very energetically suitable. According to Fig. 3(a), the top of In–S is the favored site for SO_2. The adsorption distance for SO_2 is 2.153 Å. It can be seen from Fig. 4(a) that charge is slightly depleted on the In and Te atoms in the monolayer, while it is accumulated on the S atom and the bonds between In–S, In–Te, and In–In. For the other five adsorption configurations, the charge is similarly accumulated and depleted on the In_2STe monolayer. Additionally, Fig. 4(a) exhibits that electrons have completely collected on SO_2. Strong SO_2 chemisorption on Janus In_2STe is suggested by the large adsorption energy and short adsorption distance.

3.2.2 NO_2. The small adsorption energy of −0.362 eV of NO_2 adsorption on In_2STe confirms weak adsorption. The top of S is the best position for NO_2 to adsorb (Fig. 3(b)). For NO_2, the adsorption distance was found to be 3.47 Å. 2 oxygen atoms in the NO_2 gas gain electrons. But electrons are depleted from the N atom, as seen in Fig. 4(b). Weak adsorption energy and a massive adsorption distance suggest that NO_2 adsorption results in a weak physisorption on the In_2STe monolayer.

3.2.3 H_2S. Weak adsorption of H_2S is indicated by the low adsorption energy (−0.119 eV). The most optimal site for H_2S adsorption is over the In–S bridge (Fig. 3(c)). The H_2S molecule's surface-to-molecule distance was 3.41 Å. Fig. 4(c) illustrates how charge is slightly depleted on the S atom and collected on two H atoms. The charge density difference illustrates how electrons redistribute when the H_2S molecule adsorbs on the surface, rather than showing absolute atomic charges from population analysis. The apparent charge accumulation near the H atom originates from polarization and charge rearrangement at the molecule–surface interface in periodic DFT calculations.[35,36] This effect reflects the influence of Janus In_2STe on the electronic distribution of the adsorbed molecule and does not indicate a change in the intrinsic electronegativity of sulfur in isolated H_2S. The physisorption of H_2S on Janus In_2STe is suggested by the long adsorption distance, small adsorption energy, and negligible charge transfer.

3.2.4 CO_2. The poor adsorption energy (−0.238 eV) measured from CO_2 adsorption on the monolayer indicates that CO_2 is weakly adsorbed on the In_2STe monolayer. The top site of In–S is considered the most favorable position for CO_2 adsorption (Fig. 3(d)). The CO_2 adsorption distance was 3.584 Å. This gas increases electrons on 2 oxygen atoms but decreases the electrons on carbon atoms, as seen in Fig. 4(d). The physisorption of CO_2 on Janus In_2STe is suggested by the large adsorption distance, weak adsorption energy, and limited charge transfer.

3.2.5 NH_3. The relatively low adsorption energy (−0.176 eV) for NH_3 indicates weak adsorption behavior. The top of In is the ideal location for NH_3 to adsorb (Fig. 3(e)). NH_3 has an adsorption distance of 3.22 Å. Electrons have considerably depleted on hydrogen but accumulated on nitrogen (Fig. 4(e)). NH_3's physisorption on In_2STe is supported by negligible adsorption energy, large adsorption distance, and little charge transfer.

3.2.6 HCN. The small adsorption energy of −0.076 eV resulting from HCN adsorption on Janus In_2STe suggests very poor adsorption. The most favorable site for HCN gas adsorption is at the top of the Te atom (Fig. 3(f)). However, the adsorption distance for HCN was determined to be 3.28 Å. In HCN gas, a considerable charge has accumulated on N and depleted on the C atom, as seen in Fig. 4(f). The H atom also has a slight accumulation of charge. HCN is physisorbed on In_2STe based on the high adsorption distance and extremely low adsorption energy.

In practical sensing devices, surface defects are often unavoidable and can influence adsorption behavior, charge transfer, and carrier transport properties. In this work, the simulations were performed on a pristine In_2STe surface to establish the intrinsic sensing characteristics. A systematic investigation of defect-related effects would require modeling various defects (creating a vacancy or doping). However, this is beyond the scope of this work because of limitations in the computational resources. Future studies may explore defect engineering and its influence on adsorption energy and sensing performance to provide a more comprehensive understanding of realistic device behavior.

3.3 Chemiresistive sensitivity and recovery characteristics of Janus In_2STe

The electronic structures of the Janus In2STe change following gas adsorption. Band spectra and PDOS have been analyzed. Fig. 5 shows the band structures of each adsorbed structure, and Fig. SI1 shows the PDOS. Following SO_2 adsorption, the band gap declined by 0.706 eV due to considerable changes in the electronic structure of the In_2STe (Fig. 5(a)). Electrical conductivity is also affected by a significant change in the bandgap. A significant degree of fluctuation in the In_2STe monolayer's conductivity is responsible for the sensitivity. Among other things, it can be used as a chemiresistive SO_2 sensor. Pronounced hybridization occurs upon SO_2 adsorption on Janus In_2STe. Fig. SI1(a) exhibits that SO_2 adsorption on In_2STe introduces strong hybridized p-states primarily between −1.5 eV and 0 eV relative to the Fermi level, with a prominent SO_2-p peak pinned close to −0.2 eV to 0 eV. This results in significant electron withdrawal from the substrate, characteristic of strong acceptor chemisorption, and adsorption energies

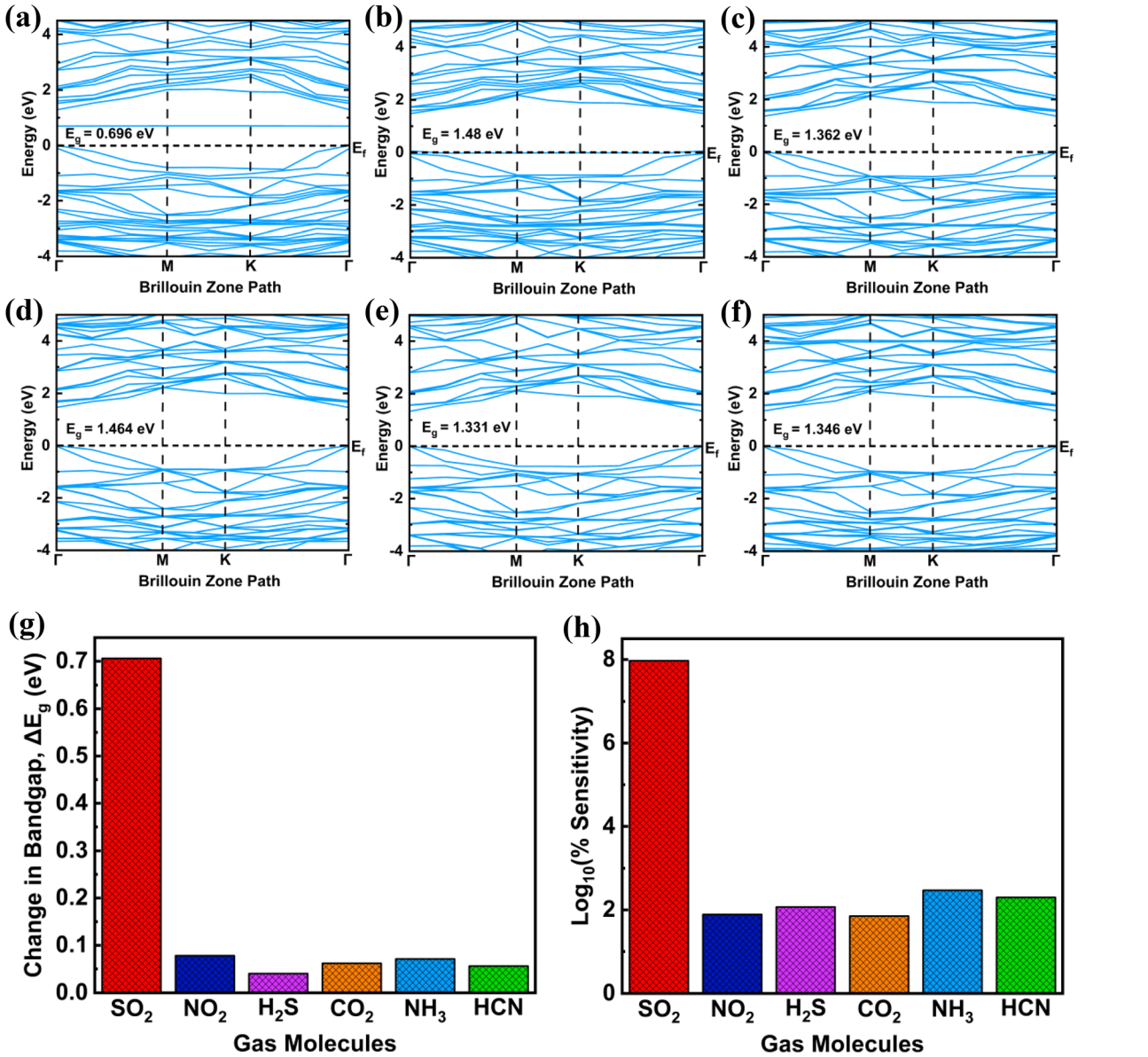

Fig. 5 The electronic band structures of In_2STe under the adsorption of (a) SO_2, (b) NO_2, (c) H_2S, (d) CO_2, (e) NH_3, and (f) HCN molecules; (g) absolute change in the bandgap (ΔE_g) and (h) logarithmic sensitivity of the In_2STe monolayer for different adsorbed gases.

estimated from −0.8 to −1.6 eV. Janus In_2STe's electronic structure was barely affected by NO_2 adsorption, as seen in Fig. 5(b), which only slightly increased the electronic bandgap by 0.078 eV. However, NO_2 causes a substantial PDOS modification, generating sharp and intense NO_2-p states pinned directly at the Fermi level (0 eV), with additional features extending slightly below to about −0.5 eV (Fig. SI1(b)). The electronic structure of In_2STe remained almost the same after H_2S adsorption. As seen from Fig. SI1(c), H_2S exhibits a much weaker effect, with gas-related states appearing well below the Fermi level, roughly in the −2.5 eV to −1 eV range. Little to no PDOS increase occurs at or near 0 eV, reflecting negligible charge transfer and mostly physisorption interaction. It can be seen from Fig. 5(c) that the band gap shift under H_2S adsorption is very negligible (0.04 eV). The electronic structure of Janus In_2STe was altered by CO_2 adsorption. CO_2 is similar to H_2S, with gas states largely confined to below −2 eV and no significant modulation near the Fermi energy level (Fig. SI1(d)). This confirms weak physisorption and limited sensor response. The bandgap increased by 0.062 eV due to CO_2 adsorption, as seen in Fig. 5(d). The In_2STe monolayer's electronic structure stayed almost the same after NH_3 adsorption. This leads to a minimal decline of 0.071 eV in band gap (Fig. 5(e)). NH_3 causes small donor-like perturbations near the conduction band edge, appearing as shallow states spanning roughly −0.3 eV below to around +0.3 eV higher than the Fermi level (Fig. SI1(e)). Janus In_2STe's electronic structure was very slightly altered upon HCN adsorption, resulting in a slight bandgap reduction of 0.056 eV (Fig. 5(f)). HCN introduces intermediate p-like states just below the Fermi level, centered between about −0.4 eV and 0 eV,

Table 1 Adsorption sites of the most energetically suitable gas adsorbed structures, adsorption distance (D), bandgap (E_g), absolute change in the bandgap (ΔE_g), adsorption energy (E_{ad}), adsorption type

Gas molecules	SO_2	NO_2	H_2S	CO_2	NH_3	HCN
Suitable sites	Between the In–S bond	Top of the S atom	Between the In–S bond	Between the In–S bond	Top of the In atom	Top of the Te atom
Adsorption distance D (Å)	2.153	3.47	3.41	3.584	3.22	3.28
Bandgap, E_g (eV)	0.696	1.48	1.362	1.464	1.331	1.346
Absolute change in bandgap, ΔE_g (eV)	0.706	0.078	0.04	0.062	0.071	0.056
Adsorption energy, E_{ad} (eV)	−0.82	−0.362	−0.119	−0.238	−0.176	−0.076
Adsorption type	Chemisorption	Physisorption	Physisorption	Physisorption	Physisorption	Physisorption

exhibiting moderate overlap with chalcogen p-states (Fig. SI1(f)). This indicates moderate electron-accepting character and results in measurable but less pronounced conductivity changes than SO_2. Changes in the electronic band gap are connected to the appearance of new states and big changes in the PDOS. As a result, changes in the conductivity of the In_2STe monolayer may make it possible to selectively detect gases. Table 1 shows the most energetically stable gas-adsorbed configurations. These include their preferred adsorption sites, adsorption distance (D), adsorption energy (E_{ad}), electronic band gap (E_g), band gap variation (ΔE_g), and type of adsorption. Table 1 shows that SO_2 has the biggest change in the band gap, the most energy needed to adsorb, and the shortest distance needed to adsorb compared to other gas molecules. There were no traits like this that made it possible to tell other gases apart. In this way, Table 1 demonstrates the In_2STe monolayer's selectivity towards SO_2.

The sensitivity from the band gap has been determined using eqn (4). Table 2 shows the chemiresistive sensitivities of Janus In_2STe at RT for 6 gases. The In_2STe monolayer demonstrated a massive bandgap decline of 0.706 eV following SO_2 adsorption. Because of this large drop in the band gap, SO_2 is the most sensitive (93.28×10^6%) (Table 2), while CO_2 is the least sensitive (70.09%). NH_3 and HCN also exhibited moderate sensitivities of 298.46% and 197.53%, respectively, although neither of these approached the level of sensitivity exhibited by SO_2. The bar charts illustrating the band gap variation and logarithmic sensitivity are presented in Fig. 5(g) and (h), respectively. Owing to its pronounced sensitivity to SO_2 at room temperature (RT), Janus In_2STe demonstrates strong potential as a sensor for highly sensitive and selective SO_2 detection.

The recovery periods for the gases on In_2STe were calculated using eqn (5). Table 2 includes the recovery durations for various gases at room temperature (298 K). Recovery times for gas adsorption are typically expected to fall within 1 to 100 seconds, which meets the requirements of most practical gas sensing applications.[12] If the recovery time exceeds this range, increasing the temperature is generally necessary to enhance gas desorption.[15,37] However, a quick recovery period also renders an inappropriate sensing for real-world RT detection.[4] Although a commonly used attempt frequency ($\nu_0 = 10^{12}\ s^{-1}$) is used in this work, the resulting recovery time should be viewed as an approximate estimate, while the adsorption energy provides a more fundamental measure of sensing performance. Among all the investigated gases, SO_2 exhibits the largest recovery period (74 s), making it very good for RT detection due to its intense interaction with In_2STe. In contrast, the others show recovery times in the microsecond, nanosecond, and picosecond ranges, indicating extremely rapid desorption. As a result, they are likely to desorb before effective sensing can occur, rendering them unsuitable for detection. As shown in Table 2, HCN has the shortest recovery time (1.93×10^{-11} s), highlighting its extreme unsuitability for RT detection on Janus In_2STe due to minimal adsorption on the inner surface. Although NO_2, H_2S, CO_2, and NH_3 exhibit comparatively larger recovery durations than HCN, these values are still too short to maintain stable interactions with Janus In_2STe. Thus, Janus In_2STe is efficient for SO_2 detection as SO_2's adsorption on In_2STe is very strong, causing a larger recovery period than that of other gases. This highlights the excellent selectivity of Janus In_2STe toward SO_2 gas.

Table 2 Table for change in bandgap, sensitivity, logarithmic sensitivity, and recovery time

Adsorbed gas	Absolute change in bandgap, ΔE_g (eV)	Sensitivity (%S)	Log_{10} (%S)	Recovery time (s)
SO_2	0.706	93.28×10^6	7.97	74
NO_2	0.078	78.10	1.89	1.326×10^{-6}
H_2S	0.04	117.89	2.07	1.03×10^{-10}
CO_2	0.062	70.09	1.85	1.06×10^{-8}
NH_3	0.071	298.46	2.47	9.47×10^{-10}
HCN	0.056	197.53	2.30	1.93×10^{-11}

3.4 Selectivity and dynamic response analysis of In_2STe monolayer: a COMSOL study

To examine the selectivity of the proposed Janus In_2STe monolayer-based gas sensor, COMSOL Multiphysics simulations were conducted for several common interfering gases, including SO_2, HCN, NH_3, and H_2S, each having a concentration of 50 ppm and at RT (Fig. 6(a)). The simulated response values for SO_2, HCN, NH_3, and H_2S were 17.62, 8.4, 7.4, and 3.67, respectively. Among all gases studied, the Janus In_2STe sensor exhibited the highest response toward SO_2, indicating its strong preference and excellent selectivity for this gas species. This enhanced selectivity is primarily attributed to the distinct interaction strength and charge redistribution between SO_2 and Janus In_2STe. Janus monolayer's asymmetric structure creates an intrinsic dipole moment, facilitating stronger electrostatic interactions and higher adsorption affinity for polar molecules such as SO_2. Variations in molecular polarity, bond energy, and chemical reactivity among the tested gases further contribute to the observed differences in sensor response. These results validate that the Janus In_2STe monolayer can effectively differentiate SO_2 from other ambient gases, establishing it as an excellent option for situations involving selective gas sensing.

The sensor's dynamic response characteristics were analyzed in COMSOL to evaluate its behavior under varying SO_2 concentrations. The time-dependent response ratio (R_a/R_g) was simulated for SO_2 concentrations varying from 50 ppm to 400 ppm (Fig. 6(b)). The result indicates the sensor's response rises proportionally as SO_2 concentration rises, displaying a clear linear trend across the studied range. The linear dependence between response and gas concentration (Fig. 6(c)) is described by the equation, $y = 1.214 + 0.308x$, where x indicates the SO_2 concentration (ppm), and y denotes the sensor response. The fitting yielded an R^2 value equal to 0.998, confirming excellent linearity and demonstrating the remarkable accuracy of the simulation model. The corresponding sensitivity of the sensor was calculated to be approximately 0.308 ppm^{-1}, indicating remarkable responsiveness even at low SO_2 concentrations.

Overall, the COMSOL simulation results demonstrate that the Janus In_2STe monolayer sensor exhibits outstanding selectivity, linearity, and sensitivity toward SO_2 detection in the 50 to

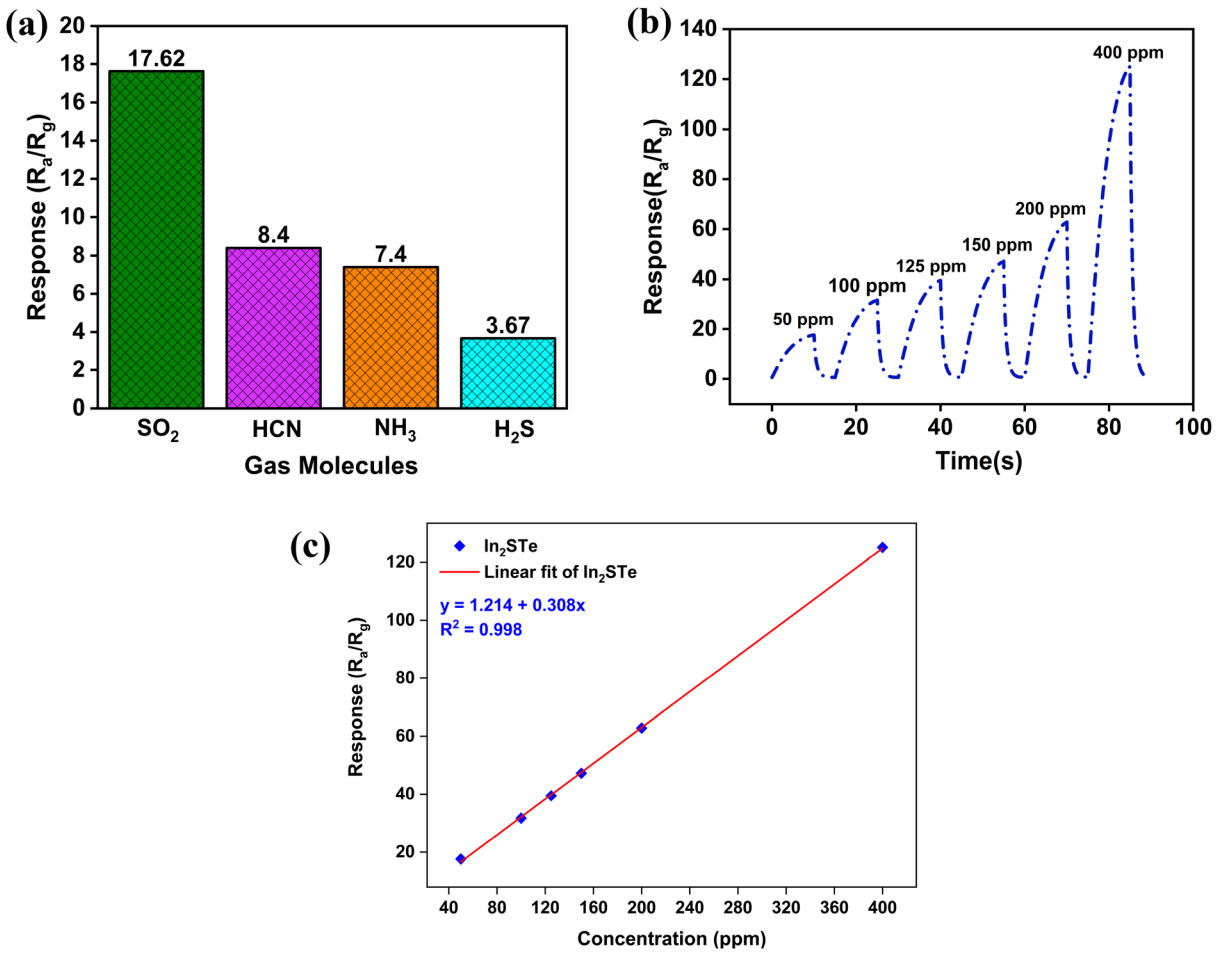

Fig. 6 (a) Selectivity comparison of In_2STe sensor towards various gases such as SO_2, HCN, NH_3, and H_2S at RT (b) dynamic response characteristics of the In_2STe sensor under exposure to different concentrations of SO_2 ranging from 50 ppm to 400 ppm at RT (c) the linear fit of the response *vs.* concentration curve for the Janus In_2STe sensor under exposure to SO_2.

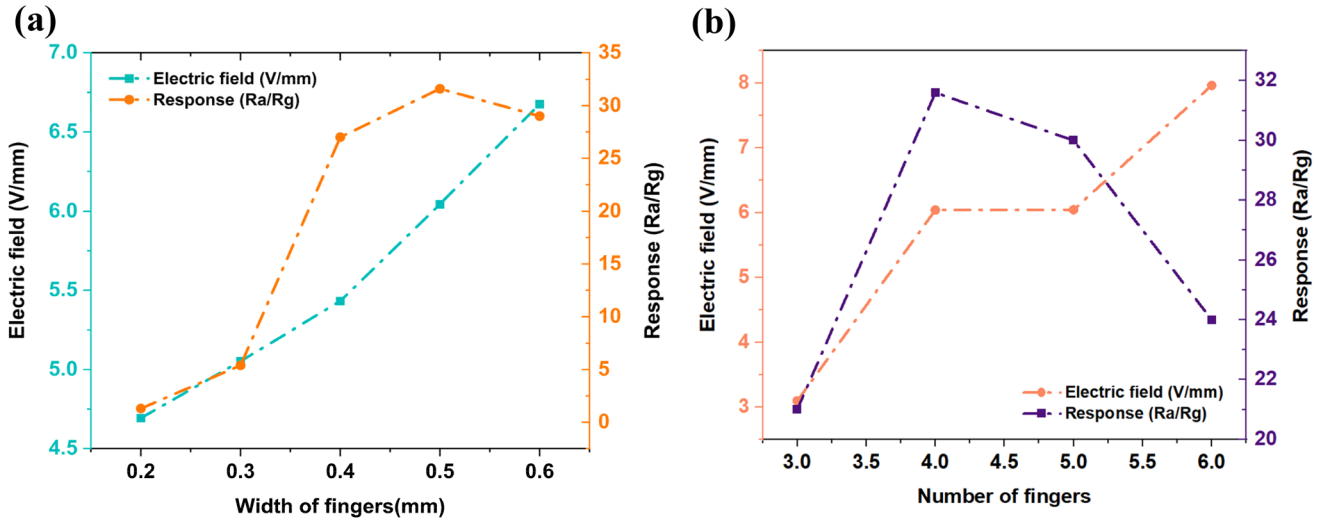

Fig. 7 (a) Maximum sensing response and the corresponding electric field of the sensor at different finger widths (b) maximum sensing response and the corresponding electric field of the sensor as a function of number of fingers.

400 ppm range. These characteristics highlight its strong potential for real-time environmental monitoring and practical applications in detecting toxic and hazardous gases.[38–40]

3.5 Optimization of interdigitated electrode geometry

To analyze the influence of width as well as the number of fingers on the performance of the proposed sensor, two sets of simulations were carried out utilizing the Electrostatics interface of the AC/DC module in COMSOL Multiphysics. A 5 V DC potential was applied between the interdigitated electrodes (IDEs), and the corresponding distributions of electric field and electric potential were visualized, as displayed in Fig. SI2(a) and SI2(b), respectively. Fig. 7(a) illustrates the variation in electric field intensity and sensor response as the finger width varies from 0.2 mm to 0.6 mm. The results reveal that both the electric field magnitude and sensor sensitivity increase with increasing finger width up to 0.5 mm. Beyond this point, at 0.6 mm, although the electric field intensity continues to rise slightly, the overall sensitivity decreases from 31.6 to 29. This enhancement in response to increasing finger width can be explained by the modulation of the metal–semiconductor interface and associated charge transport phenomena. As the finger width increases, the effective contact area between the electrode and the semiconductor expands, resulting in a more pronounced Schottky Barrier Height (SBH) at contacts. The elevated SBH induces a wider electron depletion region in the semiconductor near the electrode surface, which increases the baseline resistance (R_a). Upon SO_2 exposure, the adsorbed gas molecules further modulate the SBH, leading to a larger reduction in resistance (R_g) and, consequently, a greater relative change in resistance (R_a/R_g). Based on these findings, the IDE structure with a 0.5 mm finger width was identified as the optimal configuration and selected for the subsequent simulation study.

The impact of changing the number of IDE fingers on sensor response is depicted in Fig. 7(b). As the number of fingers increased from three to four, both the electric field strength and sensing response improved, reaching a maximum response of 31.6. However, further increasing the number of fingers resulted in a decline in sensitivity, dropping to 30 for five fingers and 24 for six fingers, forming a bell-shaped (volcanic) response trend. This characteristic can be understood in terms of the balance between baseline resistance and charge carrier concentration. When the number of fingers increases from three to four, the overall electrode area and interfacial field strength enhance charge carrier modulation, thereby improving sensitivity. In contrast, beyond four fingers, the baseline resistance decreases, leading to a higher initial carrier density. Under such conditions, the relative contribution of charge carriers induced by SO_2 adsorption becomes smaller compared to the total carrier population, resulting in a reduced change in resistance and, thus, lower response. Therefore, optimizing the number of fingers is crucial to achieving maximum sensing performance. Overall, this study offers an extensive geometric optimization of the proposed IDE structure, demonstrating that careful tuning of the finger width and finger count can significantly enhance sensor sensitivity and selectivity. In short, this research presents an extensive optimization of the geometric parameters of the proposed IDE configuration.[41–45]

4. Conclusions

To conclude, the gas adsorption behavior on the Janus In_2STe monolayer was examined by DFT computations. For six gases: SO_2, NO_2, H_2S, CO_2, NH_3, and HCN, important electronic and adsorption metrics, such as CDD, adsorption energy, band structure, PDOS, and adsorption distance, were assessed. Among these, SO_2 was chemisorbed, demonstrating the largest adsorption energy of −0.82 eV and the minimal distance (2.153 Å) to adsorb, indicating the strongest contact. The remaining

gases, on the other hand, showed physisorption. The band gap witnessed a significant decline of 0.696 eV as a result of SO_2 adsorption, indicating an extraordinarily high chemiresistive sensitivity of 93.28 × 10^6%. Charge transfer analysis showed that SO_2 acts as a charge (electron) acceptor. The Janus In_2STe monolayer also demonstrated a steady recovery time of 74 s for SO_2, exhibiting reliable detection performance. Moreover, a Janus In_2STe monolayer-based gas sensor was simulated in COMSOL Multiphysics. The simulation results confirm that the Janus In_2STe monolayer offers strong selectivity and excellent sensitivity toward SO_2, clearly distinguishing it from other common gases. The sensor exhibits a linear response across 50–400 ppm of SO_2 with an excellent sensitivity of 0.308 ppm^{-1}. Furthermore, the optimization of IDE geometry shows that a 0.5 mm finger width and four fingers yield the highest electric field strength and sensing performance. Together, these results demonstrate that both material properties and electrode design play key roles in enhancing detection capability. Overall, Janus In_2STe's improved selectivity and sensitivity demonstrate its promise as a viable option for SO_2 sensing applications.

Conflicts of interest

All authors declare that they have no conflicts of interest.

Data availability

The data supporting this article have been included as part of the supplementary information (SI). Supplementary information is available. See DOI: https://doi.org/10.1039/d5ra09962e.

Acknowledgements

We sincerely thank the Department of Electrical and Electronic Engineering of Khulna University of Engineering & Technology (KUET), Khulna-9203, Bangladesh, for their unwavering encouragement and assistance during this study. Additionally, we are grateful to the UGC Funded Research Project 2024–2025 for its financial support, which enabled our effort. We also acknowledge KUET's Central Computer Center for their invaluable assistance with software and technical support.

References

1 P. Córdoba, Emissions of Inorganic Trace Pollutants from Coal Power Generation, in *Air Pollution - Monitoring, Quantification and Removal of Gases and Particles*, IntechOpen, 2019, DOI: 10.5772/intechopen.79918.

2 M. Bala, M. T. Rahman, R. Al Nahean, B. Sorker, and M. R. Firoz, Adsorption and Gas Sensing Properties of GaAs Monolayer: A DFT Study, in *2024 13th International Conference on Electrical and Computer Engineering (ICECE)*, IEEE, 2024, pp. 74–79, DOI: 10.1109/ICECE64886.2024.11024722.

3 D. Singh and R. Ahuja, Highly Sensitive Gas Sensing Material for Environmentally Toxic Gases Based on Janus NbSeTe Monolayer, *Nanomaterials*, 2020, **10**(12), 2554, DOI: 10.3390/nano10122554.

4 K. A. Abdur Nur, M. S. Hasan Khan and M. R. Islam, Superior selectivity for NH3 (NO2) gas molecules in In2SSe (Ga2SSe) Janus materials: a first-principles study, *Phys. Scr.*, 2024, **99**(9), 095934, DOI: 10.1088/1402-4896/ad69d2.

5 A. Kandemir and H. Sahin, Janus single layers of *In 2 SSe* : A first-principles study, *Phys. Rev. B*, 2018, **97**(15), 155410, DOI: 10.1103/PhysRevB.97.155410.

6 B. Babariya, D. Raval, S. K. Gupta and P. N. Gajjar, Selective and sensitive toxic gas-sensing mechanism in a 2D Janus MoSSe monolayer, *Phys. Chem. Chem. Phys.*, 2022, **24**(25), 15292–15304, DOI: 10.1039/D2CP01648F.

7 M. Bala, M. T. Rahman, R. Al Nahean and M. S. Hasan Khan, NO $_2$ and SO $_2$ adsorption and sensing on Janus B $_2$ SeTe: unveiling its electronic, optical, and magnetic properties through DFT and COMSOL, *RSC Adv.*, 2025, **15**(31), 25187–25201, DOI: 10.1039/D5RA04190B.

8 N. H. Song, Y. S. Wang, L. Y. Zhang, Y. Y. Yang and Y. Jia, Density functional theory study of tunable electronic and magnetic properties of monolayer BeO with intrinsic vacancy and transition metal substitutional doping, *J. Magn. Magn. Mater.*, 2018, **468**, 252–258, DOI: 10.1016/j.jmmm.2018.08.019.

9 N. H. Mohd Zaki, A. M. M. Ali, M. F. Mohamad Taib, W. I. N. Wan Ismail, S. Sepeai and A. Ramli, Dispersion-correction density functional theory (DFT+D) and spin-orbit coupling (SOC) method into the structural, electronic, optical and mechanical properties of CH3NH3PbI3, *Comput. Condens. Matter*, 2023, **34**, e00777, DOI: 10.1016/j.cocom.2022.e00777.

10 B. Babariya, D. Raval, S. K. Gupta and P. N. Gajjar, Selective and sensitive toxic gas-sensing mechanism in a 2D Janus MoSSe monolayer, *Phys. Chem. Chem. Phys.*, 2022, **24**(25), 15292–15304, DOI: 10.1039/D2CP01648F.

11 J. Gao, *et al.*, First principle investigation on gas sensing properties of MoS2/ZnO heterojunction, *Microchem. J.*, 2024, **206**(Nov), 111414, DOI: 10.1016/j.microc.2024.111414.

12 R. Al Nahean, M. Bala, M. T. Rahman and M. R. Firoz, Tailoring Pt-loaded MoS $_2$/SnO $_2$ heterostructures for high-sensitivity room-temperature ammonia detection: a DFT and COMSOL analysis, *J. Mater. Chem. A Mater*, 2026, **14**(19), 11689–11709, DOI: 10.1039/D5TA07648J.

13 R. Shahriar, O. Hassan and Md. K. Alam, Adsorption of gas molecules on buckled GaAs monolayer: a first-principles study, *RSC Adv.*, 2022, **12**(26), 16732–16744, DOI: 10.1039/D2RA02030K.

14 T. M. Ngoc, *et al.*, Ultralow power consumption gas sensor based on a self-heated nanojunction of SnO $_2$ nanowires, *RSC Adv.*, 2018, **8**(63), 36323–36330, DOI: 10.1039/C8RA06061D.

15 Y. He, *et al.*, Ab-Initio Study of Run and Rhn (n = 1-3) Nanoclusters on Monolayer MoSSe for Sensing Industrial Toxic Gases, *ACS Appl. Nano Mater.*, 2025, **8**(13), 6659–6670, DOI: 10.1021/acsanm.5c00458.

16 T. Anam, M. T. Rahman, L. Dong and Q. Qiao, Low-Temperature Detection of Carbon Monoxide with

Enhanced Sensitivity Using Ag-Loaded ZnO/rGO-Modeling, Simulation, and Validation, *IEEE Sens. J.*, 2024, **24**(12), 18827–18834, DOI: 10.1109/JSEN.2024.3389770.

17 R. Al Nahean, M. T. Rahman, M. R. Firoz, S. N. Shanto, and Md. S. Alam Biswas Shakin, "Au-Pt Loaded Graphene/MoS_2 Heterostructure for High-Performance NH_3 Sensing at Room Temperature," in *2024 27th International Conference on Computer and Information Technology (ICCIT)*, IEEE, 2024, pp. 132–137, DOI: 10.1109/ICCIT64611.2024.11021913.

18 M. R. Firoz, R. Al Nahean, and M. T. Rahman, "Room Temperature Detection of NH_3 at ppb Level Using Pt-Decorated ZnO/MoS_2 Heterostructures," in *2025 International Conference on Electrical, Computer and Communication Engineering (ECCE)*, IEEE, 2025, pp. 1–6, DOI: 10.1109/ECCE64574.2025.11013921.

19 Md. S. A. Biswas Shakin, S. N. Shanto, M. T. Rahman, T. Anam, B. Sorker, and T. Sazzad, "Pt/Au-Loaded ZnO Based Carbon Monoxide Sensor with Enhanced Sensitivity," in *2023 26th International Conference on Computer and Information Technology (ICCIT)*, IEEE, 2023, pp. 1–5, DOI: 10.1109/ICCIT60459.2023.10441389.

20 S. N. Shanto, M. T. Rahman, Md. S. A. B. Shakin and M. M. Rana, Enhanced Gas Sensing Properties of Au Loaded ZnO/WSe_2 Heterostructure at Room Temperature-Modeling and Simulation, *IEEE Sens. J.*, 2025, 1, DOI: 10.1109/JSEN.2025.3585409.

21 M. S. A. B. Shakin, M. T. Rahman, S. N. Shanto and M. M. Rana, Au-Loaded WS2/SnO2 Heterostructure for Room Temperature Detection of CO at ppb-Level, *IEEE Sens. J.*, 2024, **24**(22), 36386–36392, DOI: 10.1109/JSEN.2024.3467052.

22 F. Lux, Models proposed to explain the electrical conductivity of mixtures made of conductive and insulating materials, *J. Mater. Sci.*, 1993, **28**(2), 285–301, DOI: 10.1007/BF00357799.

23 V. Šnejdar and J. Jerhot, Electrical conductivity of polycrystalline semiconductors, *Thin Solid Films*, 1976, **37**(3), 303–316, DOI: 10.1016/0040-6090(76)90600-3.

24 M. Caglar, Y. Caglar, S. Aksoy and S. Ilican, Temperature dependence of the optical band gap and electrical conductivity of sol–gel derived undoped and Li-doped ZnO films, *Appl. Surf. Sci.*, 2010, **256**(16), 4966–4971, DOI: 10.1016/j.apsusc.2010.03.010.

25 W. Chen, Q. Zhou, F. Wan and T. Gao, Gas sensing properties and mechanism of Nano-SnO2-based sensor for hydrogen and carbon monoxide, *J. Nanomater.*, 2012, **2012**, 612420, DOI: 10.1155/2012/612420.

26 A. Marjaoui, M. Ait Tamerd, B. Abraime, A. El Kasmi, M. Diani and M. Zanouni, The electronic, thermoelectric and optical properties of Janus In2STe monolayer: A first-principles investigation, *Thin Solid Films*, 2022, **759**, 139471, DOI: 10.1016/j.tsf.2022.139471.

27 A. Hedler, S. L. Klaumünzer and W. Wesch, Amorphous silicon exhibits a glass transition, *Nat. Mater.*, 2004, **3**(11), 804–809, DOI: 10.1038/nmat1241.

28 J. H. Choi, *et al.*, Nearly single-crystalline GaN light-emitting diodes on amorphous glass substrates, *Nat. Photonics*, 2011, **5**(12), 763–769, DOI: 10.1038/nphoton.2011.253.

29 R. Al Nahean, M. Bala, M. T. Rahman and R. Firoz, Tailoring Pt-Loaded MoS2/SnO2 Heterostructures for High-Sensitivity Room-Temperature Ammonia Detection: A DFT and COMSOL Analysis, *J. Mater. Chem. A Mater*, 2026, **14**(19), 11689–11709, DOI: 10.1039/D5TA07648J.

30 M. Bala, M. T. Rahman and N. Goswami, Tailoring Janus In_2SeTe monolayers with Al doping: a computational study for NO_x sensing applications, *RSC Adv.*, 2025, **15**(45), 38406–38421, DOI: 10.1039/D5RA05591A.

31 S. Saha, D. I. Sajib and Md. K. Alam, Interaction of the III-As monolayer with SARS-CoV-2 biomarkers: implications for biosensor development, *Phys. Chem. Chem. Phys.*, 2024, **26**(7), 6242–6255, DOI: 10.1039/D3CP05215J.

32 A. Kushwaha and N. Goel, A DFT study of superior adsorbate–surface bonding at Pt-WSe2 vertically aligned heterostructures upon NO2, SO2, CO2, and H2 interactions, *Sci. Rep.*, 2024, **14**(1), 15708, DOI: 10.1038/s41598-024-65213-y.

33 U. Burghaus, Surface chemistry of CO2 – Adsorption of carbon dioxide on clean surfaces at ultrahigh vacuum, *Prog. Surf. Sci.*, 2014, **89**(2), 161–217, DOI: 10.1016/j.progsurf.2014.03.002.

34 R. S. Dima, D. M. Tshwane, K. Shingange, R. Modiba, N. E. Maluta and R. R. Maphanga, Adsorption of NH3 and NO2 Molecules on Sn-Doped and Undoped ZnO (101) Surfaces Using Density Functional Theory, *Processes*, 2022, **10**(10), 2027, DOI: 10.3390/pr10102027.

35 A. Klamt, J. Reinisch, F. Eckert, A. Hellweg and M. Diedenhofen, Polarization charge densities provide a predictive quantification of hydrogen bond energies, *Phys. Chem. Chem. Phys.*, 2012, **14**(2), 955–963, DOI: 10.1039/C1CP22640A.

36 P. A. Johnson, L. J. Bartolotti, P. W. Ayers, T. Fievez, and P. Geerlings, "Charge Density and Chemical Reactions: A Unified View from Conceptual DFT," in *Modern Charge-Density Analysis*, Dordrecht: Springer Netherlands, 2011, pp. 715–764, DOI: 10.1007/978-90-481-3836-4_21.

37 H. Xie, G. Lin, H. Wu, J. Zeng, L. Chen and T. Jiang, Adsorption and gas sensing properties of Cun, Agn and Rhn (n=1–3) clusters doped with WTe2 for transformer winding deformation fault gases, *Colloids Surf. A Physicochem. Eng. Asp.*, 2025, **704**, 135550, DOI: 10.1016/j.colsurfa.2024.135550.

38 K. A. Abdur Nur, M. S. Hasan Khan and M. R. Islam, Superior selectivity for NH3 (NO2) gas molecules in In2SSe (Ga2SSe) Janus materials: a first-principles study, *Phys. Scr.*, 2024, **99**(9), 095934, DOI: 10.1088/1402-4896/ad69d2.

39 F. Yaghouti Niyat and M. H. Shahrokh Abadi, COMSOL-Based Modeling and Simulation of SnO2/rGO Gas Sensor for Detection of NO2, *Sci. Rep.*, 2018, **8**(1), 2149, DOI: 10.1038/s41598-018-20501-2.

40 M. Bala, M. T. Rahman, R. Al Nahean and M. S. Hasan Khan, NO2 and SO2 adsorption and sensing on Janus B2SeTe: unveiling its electronic, optical, and magnetic properties

through DFT and COMSOL, *RSC Adv.*, 2025, **15**(31), 25187–25201, DOI: 10.1039/d5ra04190b.

41 V. R. Naganaboina, S. Bonam, M. Anandkumar, A. S. Deshpande and S. G. Singh, Improved chemiresistor gas sensing response by optimizing the applied electric field and interdigitated electrode geometry, *Mater. Chem. Phys.*, 2023, **305**(Sep), 127975, DOI: 10.1016/j.matchemphys.2023.127975.

42 A. Y. Ahmed, F. M. F. Baskaran, A. A. S Rabih, J. O. Dennis, M. H. Md Khir and M. A. A. Elmaleeh, Design, Modeling and Simulation of Microhotplate for Application in Gas Detection, *2018 International Conference on Intelligent and Advanced System (ICIAS)*, Kuala Lumpur, Malaysia, 2018, pp. 1–5, DOI: 10.1109/ICIAS.2018.8540620.

43 A. Falak, *et al.*, Room Temperature Detection of NO2 at ppb Level and Full Recovery by Effective Modulation of the Barrier Height for Titanium Oxide/Graphene Schottky Heterojunctions, *Adv. Mater. Interfaces*, 2019, **6**(22), 1900992, DOI: 10.1002/admi.201900992.

44 R. A. Kraya and L. Y. Kraya, The role of contact size on the formation of Schottky barriers and ohmic contacts at nanoscale metal-semiconductor interfaces, *J. Appl. Phys.*, 2012, **111**(6), DOI: 10.1063/1.3693542.

45 N. Hikmah, H. F. Hawari and M. Gupta, Design and simulation of interdigitated electrode for GrapheneSnO2 sensor on acetone gas, *Indones. J. Electr. Eng. Comput. Sci.*, 2020, **19**(1), 119–125, DOI: 10.11591/ijeecs.v19.i1.pp119-125.